Molecular Catalysis 601 (2026) 116190

Contents lists available at ScienceDirect

Molecular Catalysis

journal homepage: www.journals.elsevier.com/molecular-catalysis

Research Paper

Potassium-promoted Fe-based catalysts for the Reverse Water-Gas Shift Reaction: Enhanced performance and suppression of surface carbon formation

Rajvikram Singh [a], Welman C. Elias [b], Byeong Jun Cha [b,c,d], Raghvendra Singh [a], Michael S. Wong [b,e,f,g,h,*], Goutam Deo [a,**]

[a] Department of Chemical Engineering, Indian Institute of Technology Kanpur, Kanpur, 208016, India
[b] Department of Chemical and Biomolecular Engineering, Rice University, 6100 Main Street, Houston, TX, 77005, USA
[c] Department of Chemistry, Sungkyunkwan University, 2066 Seobu-ro, Suwon, Gyeonggi-do, South Korea
[d] Department of Fine Chemistry, Seoul National University of Science and Technology, 232 Gongneung-ro, Seoul, South Korea
[e] Department of Civil and Environmental Engineering, Rice University, 6100 Main Street, Houston, TX, 77005, USA
[f] Department of Materials Science and NanoEngineering, Rice University, 6100 Main Street, Houston, TX, 77005, USA
[g] Rice Water Institute, Rice University, 6100 Main Street, Houston, TX, 77005, USA
[h] Rice Advanced Materials Institute, Rice University, 6100 Main Street, Houston, TX, 77005, USA

ARTICLE INFO

Keywords:
RWGS
Fe/ZrO_2 catalysts
K-promotion
Syngas
Fe monolayer coverage

ABSTRACT

Carbon dioxide (CO_2) is a major greenhouse gas that contributes significantly to global warming and its utilization to produce a valuable product is a potential approach to mitigate emissions. The reverse water gas shift (RWGS) reaction is a promising method to convert CO_2 into synthesis gas upon high-temperature reaction with hydrogen. In this study, iron-based catalysts supported on ZrO_2 were synthesized using incipient wetness impregnation (IWI) method to identify the effect of metal loading based on carbon monoxide (CO) yield and carbon formation. The catalyst near monolayer coverage ($\sim$ 6.0 $atom_{Fe}/nm^2$), with 2.5 wt.% Fe loading demonstrates highest CO yield and low carbon formation compared to other loadings. To enhance its performance and stability, the catalyst was promoted with potassium (K) at different K:Fe molar ratio (K/Fe = 0.05, 0.10, 0.15 and 0.20). Characterization techniques, including Raman spectroscopy, BET analysis, and thermogravimetric analysis (TGA), revealed that K addition significantly increased catalytic activity and suppressed carbon formation on the surface. H_2-TPR and XPS spectra confirmed that K increased the amount of reducible surface Fe content. However, excess K (beyond a 0.10 molar ratio) led to the coverage of active sites and the formation of non-reducible Fe species, leading to lower catalytic activity. The 2.5Fe0.05 K retained nearly 98% of its initial activity after 48 h at 550 °C and atmospheric pressure. This catalyst shows great promise for RWGS reactions, paving the way for further exploration of the reaction mechanism.

1. Introduction

Global warming poses one of the greatest threats to sustainable development, primarily driven by the continuous rise in greenhouse gas (GHG) emissions. Among these gases, carbon dioxide (CO_2) is the dominant contributor, responsible for over 60% of the total radiative forcing [1]. The atmospheric concentration of CO_2 has increased from approximately 280 ppm in the pre-industrial era to over ~425 ppm in 2024, and it is projected to double within the next few decades if effective mitigation strategies are not implemented [2].

Various approaches have been proposed to reduce atmospheric CO_2 levels. These approaches include: (i) transition to renewable energy sources, (ii) carbon capture and storage (CCS), and (iii) CO_2 utilization [3–5]. While renewable energy adoption is accelerating, the complete replacement of fossil fuels remains economically and technically challenging. Therefore, attention has increasingly turned toward carbon capture and utilization (CCU) – transforming CO_2 into value-added products and fuels [6,7]. Among different utilization strategies,

* Corresponding author at: Department of Chemical and Biomolecular Engineering, Rice University, 6100 Main Street, Houston, TX, 77005, USA.
** Corresponding author.
E-mail addresses: mswong@rice.edu (M.S. Wong), goutam@iitk.ac.in (G. Deo).

https://doi.org/10.1016/j.mcat.2026.116190
Received 7 May 2026; Received in revised form 22 June 2026; Accepted 1 July 2026
Available online 4 July 2026
2468-8231/© 2026 Elsevier B.V. All rights are reserved, including those for text and data mining, AI training, and similar technologies.

3.2. X-ray diffraction

The XRD pattern of pretreated catalyst samples are shown in the range of 2θ= 25° to 55°. The XRD pattern of first set of catalysts, xFeZr, where x = 0.0, 1.0, 2.0, 2.5, 3.0 and 5.0, is shown in Fig. 1(A). All the calcined samples exhibit the XRD diffraction pattern predominantly due to the monoclinic (m-ZrO_2) phase, with characteristic peaks identified at 2θ= 24.2°, 28.2°, 31.5°, 34.4°, 38.7°, 40.9°, 45.5° and 49.4° [42,43]. The tetragonal (t-ZrO_2) phase, with characteristic peaks of t-ZrO_2 are identified at 2θ= 35.35°, 50.25° and 54.1° [44,45], is barely detectable. However, the t-ZrO_2 phase may be present with crystallite sizes that are smaller than those that can be detected by XRD. The intensity of m-ZrO_2 and t-ZrO_2 peaks are similar in all the xFeZr samples. The XRD patterns of the xFeZr catalysts show no noticeable change compared to pure ZrO_2, indicating that the incorporation of Fe does not alter the crystalline structure of the zirconia support. This suggests that Fe species are highly dispersed on the ZrO_2 surface. There is no additional peak due to addition of Fe until 2.5% metal loading. It shows that the Fe is uniformly dispersed over ZrO_2 surface. The addition of Fe above 2 wt.% starts showing a very minor peak at 2θ= 33.3°, which is corresponding to Fe_2O_3 species [46–48]. The intensity of this peak increases with increase in Fe metal loading. It shows that the Fe_2O_3 crystals starts forming between 2 and 2.5 wt.% of Fe metal loading. The monolayer coverage of Fe on this ZrO_2 lies between 4.5 – 5.6 $atom_{Fe}/nm^2$ based on XRD results and BET surface area analysis, it is similar to the Fe monolayer coverage reported on CeO_2 [49].

The XRD pattern of 2.5FeyK, where y = 00, 0.05, 0.10, 0.15 and 0.20, are shown in Fig. 1(B). There is no visible change in the XRD pattern of ZrO_2 peaks in any of the samples, suggesting that there is no major structural change occurring with the support due to K addition. It should be noted that the very minor peak at 2θ= 33.3° in the spectra of 2.5FeZr disappeared when K was added. It appears that the addition of K increased the dispersion of Fe oxide species on the ZrO_2 surface.

A zoomed in XPS spectra of xFeZr and 2.5FeyK in the range of 2θ= 32.9° to 33.5° is shown in Fig. S2 of Supplementary Information File. The Fig. S2(A) shows that the additional peak due to Fe_2O_3 species starts showing up above 2% metal loading and its intensity increases with increase in metal loading. The Fig. S2(B) shows that addition of K in 2.5FeZr catalytic system. It shows that addition of K vanishes the peak due to Fe_2O_3 species.

The XRD pattern of some of the calcined and reduced samples are shown in Fig. S3 of supplementary information file. The characteristic peaks analogous to ZrO_2 remains unchanged in calcined and spent samples. An interesting observation is made that the very minor peak due to Fe_2O_3 at 2θ= 33.3° in calcined sample of 2.5FeZr vanishes in the reduced sample. The absence of this peak suggests that the Fe^{+3} species was either successfully reduced to lower oxidation state, or it is not detectable upon reduction.

3.3. UV–vis spectroscopy

The UV–vis diffused reflectance spectra of all the prepared catalysts were recorded under ambient conditions in the wavelength range of 200–800 nm. The ZrO_2 support was used as the reference background to accurately evaluate the influence of Fe loading and K promotion on the electronic structure of the catalysts. The spectra of the first set of catalysts, designed to examine the effect of Fe loading are presented in Fig. 2. Four major bands in this set of catalysts are observed at 275, 350, 475 and 540 nm. The characteristic band at 275 nm represents the isolated octahedral Fe^{+3} species, especially in low loadings [41,50,51]. This band is evident in all the samples. The band around 350 nm shows the presence of dispersed Fe^{+3} species [41,50,52]. This band grows with metal loading and later plateaus out. The pronounced and broadened absorption band cantered at around 480 nm can be attributed to extra-framework FeO_X oligomers or iron oxide phases [53]. The intensity of this band increases progressively with metal loading and eventually reaches a plateau. And the band around 550 nm is the characteristic band of α-Fe_2O_3 [50,54,55]. This band was not visible in 1FeZr and then it starts with Fe loading growing from 2FeZr onwards.

The UV–vis spectra of the second set of catalysts, synthesized to investigate the effect of potassium promotion, are shown in Fig. S4 of Supplementary Information File. The incorporation of varying potassium loadings into the 2.5FeyK (y = 0.00, 0.05, 0.10, 0.15 and 0.20) catalysts does not induce significant overall spectral changes. However, the absorption band at ~350 nm, attributed to Fe^{+3} species, progressively intensifies with increasing K content, indicating enhanced dispersion of Fe^{+3} species. Concurrently, the characteristic absorption feature of α-Fe_2O_3 at ~540 nm diminishes upon K addition. These trends suggest that potassium promotion favours the formation of highly dispersed Fe^{+3} species while suppressing the growth of bulk α-Fe_2O_3 domains, consistent with the absence of corresponding diffraction features in the XRD patterns.

3.4. X-ray photoelectron spectroscopy (XPS)

The Fe 2p XPS spectra of the freshly calcined 1FeZr, 2.5FeZr, and 2.5Fe0.05 K catalysts are presented in Fig. 3. All samples exhibit Fe 2p features characteristic of mixed Fe^{+2} and Fe^{+3} oxidation states, with no detectable contribution from metallic Fe^0. Well-defined satellite structures associated with both oxidation states are clearly observed. The

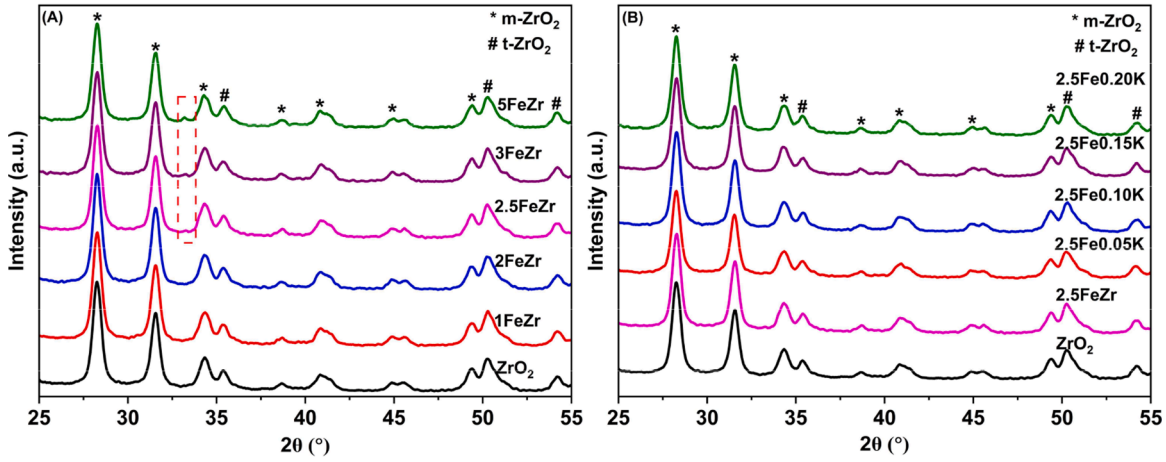

Fig. 1. XRD pattern of ZrO_2 supported catalysts, (A) xFeZr catalyst showing the effect of metal oxide loading, x = 1.0, 2.0 2.5, 3.0 and 5.0 and (B) 2.5FeyK catalyst showing the effect of potassium addition, y = 0.00, 0.05, 0.10, 0.15 and 0.20.

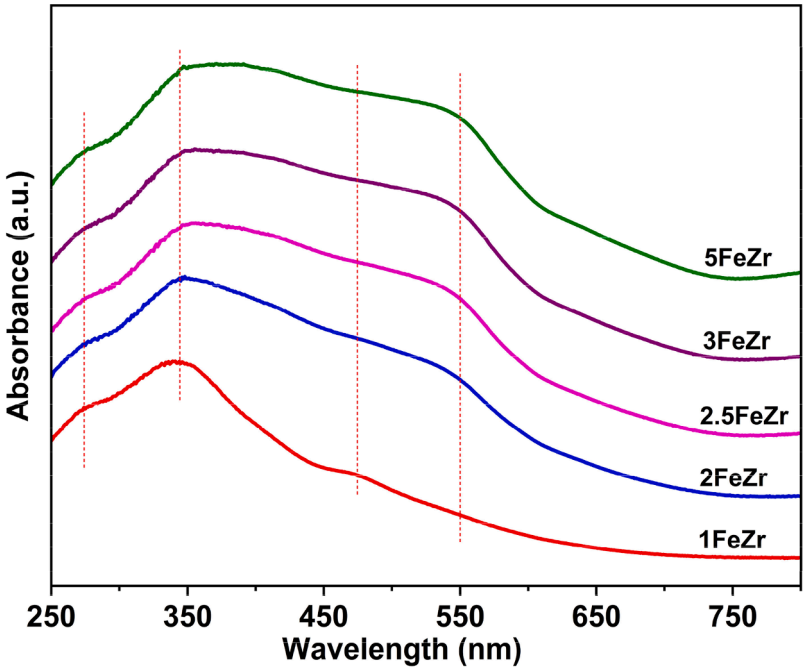

Fig. 2. UV–vis spectra of ZrO_2 supported iron catalyst, xFeZr, showing the effect of metal oxide loading, x = 1.0, 2.0 2.5, 3.0 and 5.0.

Fe^{+2} species are identified by Fe $2p_{3/2}$ and Fe $2p_{1/2}$ peaks at binding energies of 709.05 and 722.05 eV, respectively, along with corresponding satellite peaks located approximately 6 eV higher, at 715.06 and 728.04 eV. In contrast, Fe^{+3} species are characterized by Fe $2p_{3/2}$ and Fe $2p_{1/2}$ peaks at 710.8 and 723.8 eV, accompanied by satellite features shifted by ~8 eV to higher binding energies, appearing at 718.8 and 731.7 eV, which is tabulated in Table S2 of Supplementary Information File. All these peaks are in agreement with reported literature values [56,57]. A comparison of Fe 2p spectra reveals that increasing the Fe loading from 1 wt. % to 2.5 wt. % results in a relative decrease in the intensity of Fe^{+3} species, accompanied by an increase in the contribution from Fe^{+2}, indicating a lower fraction of Fe^{+3} at higher metal loadings. The ratio of Fe^{+3}/Fe^{+2} is 3.28 for 1FeZr and it decreased to 1.65 for 2.5FeZr. In contrast, potassium promotion leads to a pronounced increase in the relative intensity of Fe^{+3} species, suggesting that K addition stabilizes higher oxidation-state iron species on the ZrO_2 support. The ratio of Fe^{+3}/Fe^{+2} is 3.51 for 2.5Fe0.05 K and it decreased to 1.65 for 2.5FeZr.

3.5. H_2-TPR

The H_2-TPR profile of xFeZr, where x = 1, 2, 2.5, 3 and 5, is shown in Fig. 4. All the samples show a primary reduction peak (first peak), and its intensity increases with increase in metal loading. And as the metal loading increases the number of peaks starts showing up. A peak emerges at 2 wt.% loading at ~430 °C and the intensity of this peak increases with increase in metal loading and as the metal loading increases the peak shifts towards the higher temperature. It indicates that the reduction peak associated with α-Fe_2O_3 species, as the metal loading increases the intensity of this peak increases, which is similar to the XRD pattern.

Area under the H_2-TPR curve shows the amount of H_2 uptake. The amount of H_2 uptake is reported in Table 1. Based on the H_2 uptake H/Fe ratio was calculated using the methodology reported previously [41]. The H/Fe ratio is also reported in the same Table 1. The H/Fe ratio decreases with increase in metal loading, initially it was 2.9 for 1FeZr and decreases and reaches 1.7 for 3FeZr and 5FeZr. The H/Fe <3 shows that a there are remaining amounts of Fe which is non reducible. The amount of non-reducible Fe increases above 2%Fe loadings, which may be corresponding to Fe_2O_3 crystallites, which are non-reducible.

The H_2 TPR profile of 2.5FeZr and 2.5FeyK, where y = 0.05, 0.10, 0.15 and 0.20, is shown in Fig. 5. All samples show multiple reduction peaks similar to 2.5FeZr. The intensity of peaks started increasing as K was added to the system and the amount of H_2 uptake starts increasing which is mentioned in Table 1. It shows that the reducible amount of Fe starts increasing with addition of K and after a certain amount it saturates. The H/Fe ratio significantly increase from 1.8 to 2.14 at a Fe to K molar ratio of 1:0.05 and further addition of K start decreasing the reducibility. Hence, the H/Fe ratio also decreases. The decrease in H/Fe ratio may be because K starts forming a stable complex with Fe, such as $KFeO_2$, which is very stable and difficult to reduce [58].

The XPS analysis has shown that as the metal loading increases from 1FeZr to 2.5FeZr, the amount of Fe^{+2} species increases, which is in accordance with H_2 TPR studies. Further addition of K in 2.5FeZr catalyst enhances the amount of Fe^{+3} species, which is also verified with the H_2 TPR studies.

3.6. Reactivity studies

Before performing the catalytic activity test, the mass transfer limitations were examined for both internal and external at 2FeZr catalyst. The detailed mass transfer effects have been given in the supplementary information file. The results are shown in Figs. S5 and S6 for external and internal mass transfer effects respectively. The operating conditions were selected based on these results, which are beyond mass transfer limitations.

3.6.1. Effect of Fe loading

The effect of Fe loading on the catalytic activity was examined, and the reactivity data is given in Table 2 and shown in Fig. S7 of Supplementary Information File. The Fig. S7 shows the average CO_2 conversion and CO yield over a period of 6 h. The CO_2 conversion and CO yield increase monotonically with increase in the metal loading until 2.5 wt.% and after that it starts decreasing very slowly. The CO yield is maximum at ~14.3%. The difference between CO_2 conversion and CO yield starts increasing after 2.5 wt.% loading, which indicates that the presence of α-Fe_2O_3 is not selective towards CO formation. The TOF values based on reducible amount of Fe (TOF^a) and total Fe loading (TOF^b), is given in

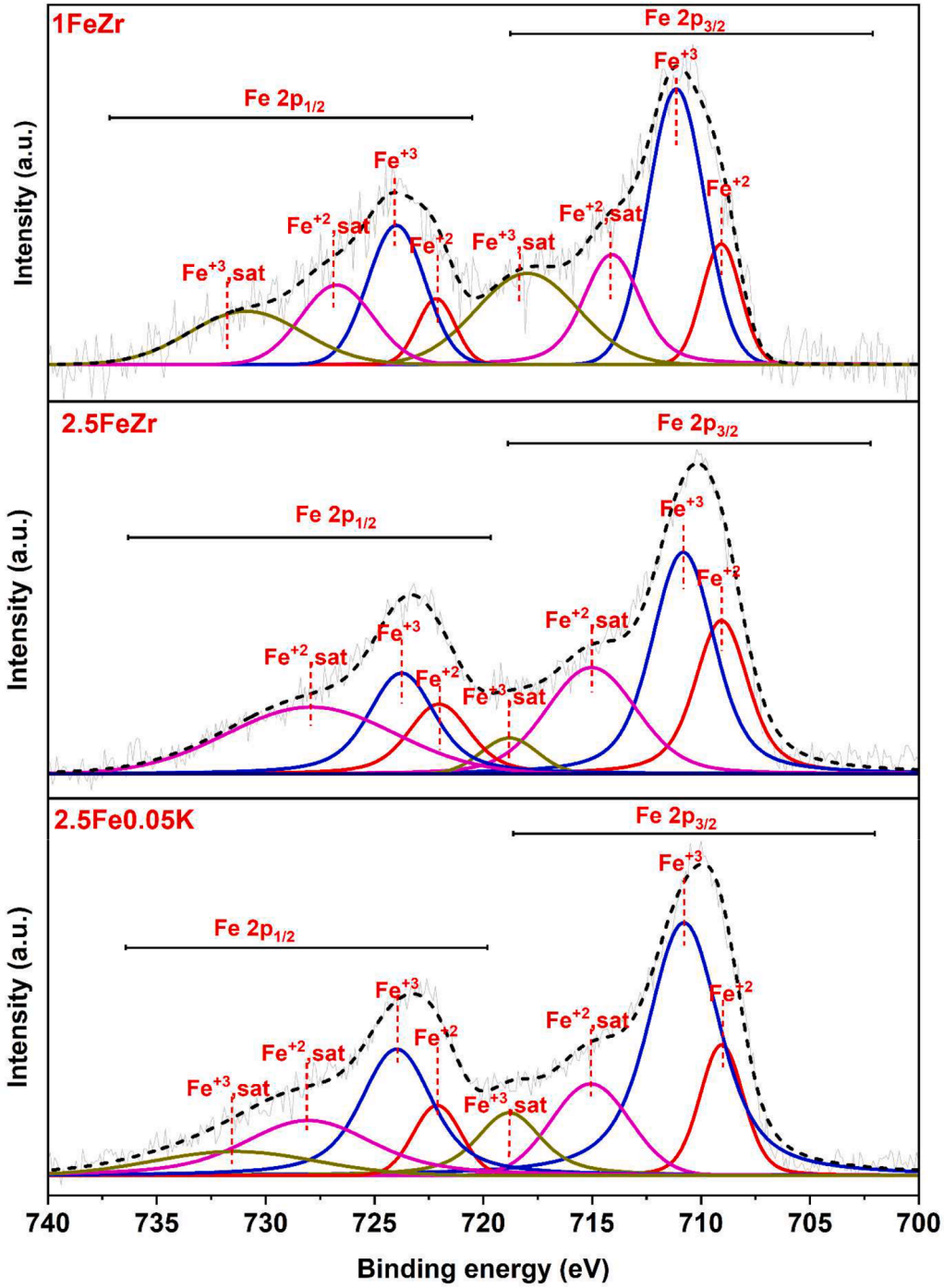

Fig. 3. Fe 2p XPS spectra of ZrO_2 supported freshly calcined 1FeZr, 2.5FeZr and 2.5Fe0.05 K.

Table 2 for CO yield. It is evident that the TOF[a] increases with increase in metal loading till 2.5FeZr and after that it starts decreasing. The TOF[a] for 1FeZr is 46.81×10^{-3} sec^{-1}, for 2.5FeZr 68.98×10^{-3} sec^{-1} and for 5FeZr it is 33.47×10^{-3} sec^{-1} at t = 0.25 h. The TOF[b] decreases with increase in metal loading monotonically. The TOF[b] for 1FeZr is 101.6×10^{-3} sec^{-1}, for [1] and for 5FeZr it is 42.6×10^{-3} sec^{-1} at t = 0.25 h.

3.6.2. *Effect of K-promotion*

The influence of potassium promotion on the RWGS activity of the 2.5FeZr catalyst was assessed by varying the K/Fe molar ratio from 0.05 to 0.20. As demonstrated in Table 3 and Fig. S8, potassium addition enhances CO formation and improves intrinsic activity relative to the unpromoted catalyst. The promotion effect is most pronounced at moderate K level (K:Fe = 0.05), which deliver the highest CO yields and superior TOF stability over the 6 h reaction period. The TOF values given in Table 3 for CO yield reveals that TOF[a] increases with increase in K/Fe ratio till 0.15 and after that it starts decreasing. The TOF[a] for 2.5FeZr is 68.98×10^{-3} sec^{-1} and for 2.5Fe0.15 K it is 75.02×10^{-3} sec^{-1} at t = 0.25 h. The TOF[b] increases with K addition till a K/Fe ratio 0.05 and further addition of K leads to decrease in TOF[b]. The TOF for 2.5Fe0.05 is 110.90×10^{-3} sec^{-1}, for and for 2.5Fe0.20 K it is 103.4×10^{-3} sec^{-1} at t = 0.25 h. This is also validated with the H_2-TPR and XPS results, which shows that addition of K enhances The Fe^{+3} species the H_2 uptake. Further addition of K appears to lead to a stronger interaction between

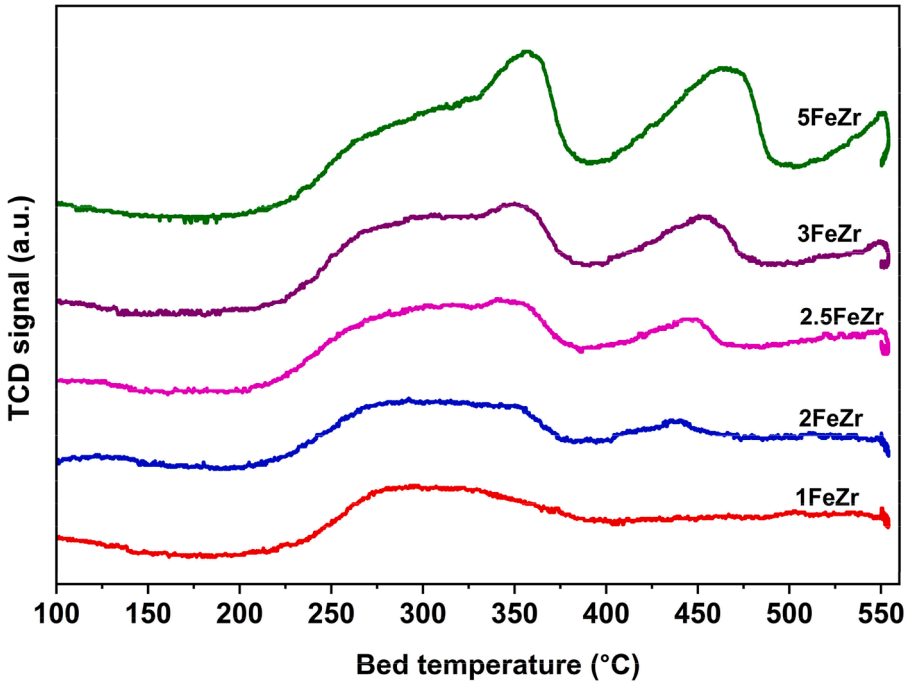

Fig. 4. H_2 TPR profile of ZrO_2 supported xFeZr catalyst showing the effect of metal oxide loading, x = 0.0, 1.0, 2.0 2.5, 3.0 and 5.0.

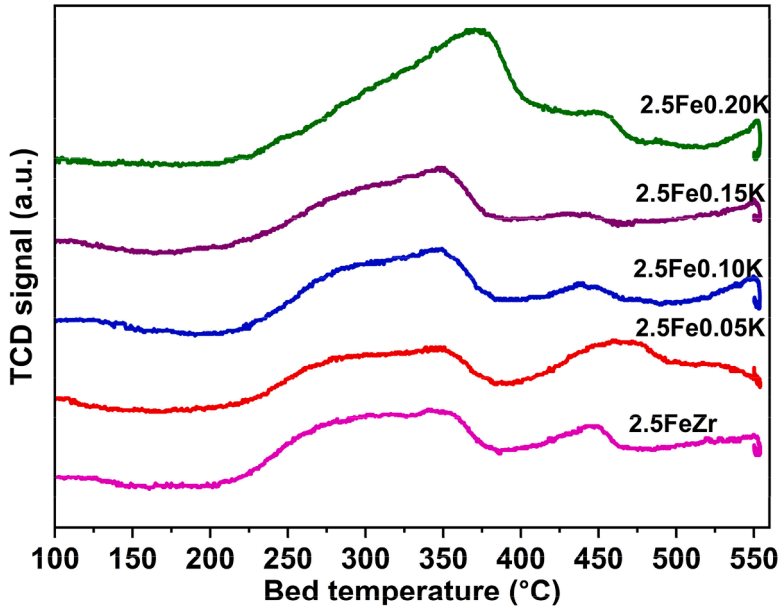

Fig. 5. H_2 TPR profile of ZrO_2 supported 2.5FeyK catalyst showing the effect of potassium addition, y = 0.00, 0.05, 0.10, 0.15 and 0.20.

Table 2
Reactivity data for xFeZr catalysts for RWGS showing the effect of loading. The ZrO_2 support is included for comparison.
Reaction conditions: $T = 550\ ^{\circ}C$ *and* $P_{H_2} = P_{CO_2} = 0.10$ *atm. and* $w = 50\ mg_{cat}$.

Catalysts	CO_2 conversion (%)		H_2 conversion (%)		CO yield (%)		$(TOF_{CO})^a * 10^{+3}\ (sec^{-1})$		$(TOF_{CO})^b * 10^{+3}\ (sec^{-1})$	
	0.25 h	6.0 h	0.25 h	6.0 h	0.25 h	6.0 h	0.25 h	6.0 h	0.25 h	6.0 h
Zr	2.09	1.92	2.11	2.01	1.76	1.82	-	-	-	-
1FeZr	6.34	6.56	6.76	6.82	6.11	6.2	46.81	47.50	101.6	103.1
2FeZr	11.98	12.26	12.21	12.58	11.52	11.70	60.95	61.90	95.7	97.2
2.5FeZr	14.48	14.60	14.52	14.68	14.15	14.25	68.98	69.47	94.1	94.7
3FeZr	13.81	13.88	13.93	14.07	13.11	13.19	57.04	57.39	72.6	73.1
5FeZr	13.04	13.13	13.33	13.43	12.82	12.89	33.47	33.65	42.6	42.9

Table 3
Reactivity data for 2.5FeyZr catalysts for RWGS showing the effect of Fe/Zr molar ratio.
Reaction conditions: The same as Table 2.

Catalysts	CO_2 conversion (%)		H_2 conversion (%)		CO yield (%)		$(TOF_{CO})^a * 10^{+3}$ (sec^{-1})		$(TOF_{CO})^b * 10^{+3}$ (sec^{-1})	
	0.25 h	6.0 h	0.25 h	6.0 h	0.25 h	6.0 h	0.25 h	6.0 h	0.25 h	6.0 h
2.5FeZr	14.48	14.60	14.52	14.68	14.15	14.25	57.04	57.39	94.1	94.7
2.5Fe0.05K	17.18	17.22	17.27	17.31	16.68	16.72	69.24	69.40	110.9	111.2
2.5Fe0.10K	16.62	16.68	16.73	16.78	16.41	16.49	72.84	73.20	109.1	109.6
2.5Fe0.15K	16.32	16.41	16.51	16.55	16.07	16.15	75.02	75.40	106.8	107.4
2.5Fe0.20K	15.63	15.61	15.72	15.68	15.55	15.52	66.64	66.51	103.4	103.2

Fe and K, and it forms thermally stable compounds (such as: $KFeO_2$). Such interactions reduce the number of reducible Fe sites, which is validated by H_2 uptake. This reflects the beneficial electronic and structural modification imparted by K. Further increases in potassium loading, however, lead to diminished catalytic performance. At a K:Fe ratio of 0.20, complete CO selectivity is achieved, yet both CO yield and turnover frequency decline. These results highlight the need for controlled potassium incorporation to optimize the balance between selectivity enhancement and sustained RWGS activity. Based on these results, the optimum catalyst was selected according to CO yield. Among all the catalysts examined, 2.5Fe0.05 K exhibited the highest CO yield and was therefore chosen for further studies.

The ZrO_2 support shows minimal CO_2 conversion and CO yield throughout the reaction, reaffirming its limited intrinsic activity. Incorporation of Fe significantly enhances performance, with 2.5FeZr achieving stable CO_2 conversions of approximately 14.5% and CO yields near 14.3%, demonstrating excellent structural and catalytic stability under reaction conditions. Potassium promotion leads to a further and consistent enhancement in RWGS activity. The 2.5Fe0.05 K catalyst exhibits the highest CO_2 conversion, maintained at approximately 17.2% over the entire TOS duration, accompanied by a proportionate increase in CO yield. The absence of appreciable performance decay highlights that the introduction of potassium not only improves CO_2 activation but also stabilizes the active phase under continuous operation.

Furthermore, the catalytic performance of the most active 2.5Fe0.05 K catalyst is compared with those reported in the literature, as summarized in Table 4. Key catalyst and reaction parameters, including catalyst composition, gas hourly space velocity (GHSV), inlet partial pressures of H_2 and CO_2, and reaction temperature, and the corresponding CO yields, are presented. The equilibrium CO yield is also included for reference. It is important to note that most literature studies were conducted at significantly lower GHSV values, which inherently favour higher conversions, and CO yields, due to longer residence times. The catalysts used in the first three rows showed CO yields near equilibrium. By lowering the GHSV our results show that the CO yield also approaches those at equilibrium. However, there are concerns of transport limitations when we conduct the experiments at lower GHSV. For the remaining catalysts the inlet partial pressure of the reactants and reaction temperature were different. Our results show that by increasing the inlet partial pressure of H_2, the CO yield increases from 17.2% to 40.22%, which approaches the results from a previous study of 54% that was obtained at lower GHSV. A decrease in reaction temperature decreases the CO yield as expected. Thus, 2.5Fe0.05 K catalyst demonstrates competitive CO yields and can be explored for further improvement in CO yield.

3.7. Contact time study

The contact study was performed in the region, which is not controlled by mass transfer limitations, keeping the reactant ratio $1\left(\frac{P_{CO_2}}{P_{H_2}}\right)$ and by changing the catalyst loading and total reactant flow rates. The results are shown in Fig. 6. It shows the effect of contact time vs CO yield at 550 °C. It shows as contact time increases, the CO yield starts increasing and it saturates at higher contact times. At the highest contact time 9.93 $g*h*mol^{-1}$ the CO yield reaches to ~34%.

3.8. Analysis of the spent catalyst

To gain deeper insight into the structural changes and surface phenomena occurring during the reaction, representative spent catalysts were analysed using XPS, Raman spectroscopy, BET surface area measurements, and thermogravimetric analysis (TGA). The XPS analysis Fe 2p spectra of spent 2.5FeZr and 2.5Fe0.05 K are shown in Fig. S9 of Supplementary Information File. The presence of Fe^{+3} and Fe^{+2} species and absence of Fe^0 species in the spent samples is evident. However, the intensity of the Fe^{+3} and Fe^{+2} peaks changes after reaction. For 2.5FeZr, the intensity ratio changed from 1.65 to 1.50 and for 2.5Fe0.05 K the change was from 3.51 to 1.90. These observations suggest that the ratio of Fe^{+3}/Fe^{+2} has decreased after reaction for both the samples.

The Raman spectra of the fresh and spent catalysts-ZrO_2, 2.5FeZr, and 2.5Fe0.05 K are presented in Fig. S10 of the Supplementary Information File. The spectra were recorded in the range of 1100–1800 cm^{-1}.

Table 4
Comparison of the different catalysts used in the literature with the most active catalyst, 2.5Fe0.05 K, used in the present study.

Catalysts and reference	GHSV $\left(\frac{mL}{g_{cat}*h}\right)$	Temperature (°C)	Partial pressure P_{H2} & P_{CO_2} (atm)	CO yield (%)	Equilibrium Conversion (%)
Pt/CeO_2 [13]	30,000	500	0.45 & 0.45	30	30.5
Fe-Cu-Cs/Al_2O_3 [17]	12,500	500	0.4 & 0.1	54	54.8
Cr/ZrO_2 [19]	22,000	600	0.45 & 0.45	38.3	37.8
Fe-K/Al_2O_3 [23]	187,500	480	0.15 & 0.15	3.5	28.9
Fe/CeO_2 [59]	60,000	500	0.4 & 0.1	50	54.8
Cs-Fe_5C_2 [60]	12,000	450	0.8 &0.2	~35	48.4
Fe-oxide [61]	6000	600	0.5 & 0.5	30	37.8
Fe–Cu/CeO_2–Al_2O_3 [62]	30,000	550	0.6 & 0.15	54	60.5
Co-Fe/Al_2O_3 [63]	60,000	550	0.3 & 0.1	30	54.9
2.5Fe0.05 K Present study	240,000	550	0.1 & 0.1	17.2	34.3
	24,000	550	0.1 & 0.1	34.2	34.3
	240,000	550	0.4 & 0.1	40.2	60.5
	240,000	500	0.4 & 0.1	32.4	54.8

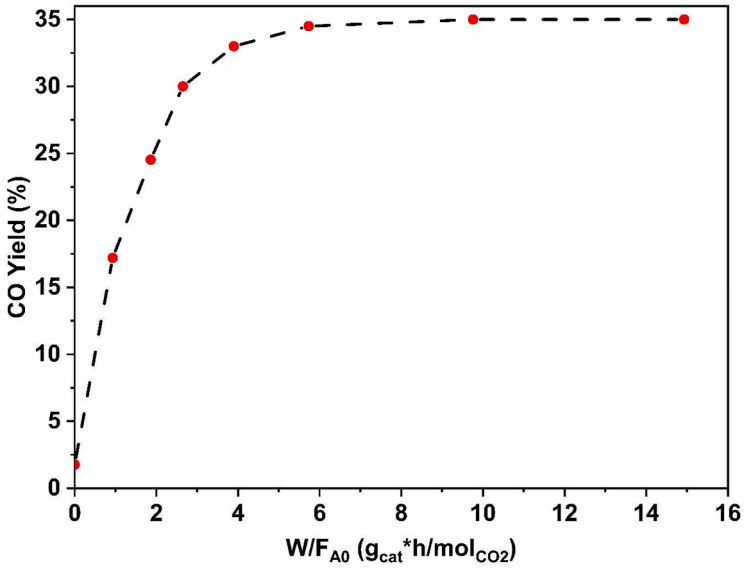

Fig. 6. CO yield for the RWGS over ZrO_2 supported 2.5Fe0.05 K catalyst showing the effect of contact time. Reaction conditions: $T = 550\ ^{\circ}C$ *and* $P_{H_2} = P_{CO_2} = 0.10$ *atm. and* $W/F_{CO_2} = 0.00 - 14.93\ g_{cat}.h/mol$.

As evident from the Fig. S10, no carbon-related features were observed in any of the fresh catalysts. The spent ZrO_2 sample exhibited a low-intensity, broad G-band around 1590 cm^{-1}, indicating minor carbonaceous deposition, while no distinct D-band was detected. In contrast, the spent 2.5FeZr catalyst displayed a weak D-band near 1310 cm^{-1} but lacked any visible G-band, suggesting limited disordered carbon formation. Notably, the spent 2.5Fe0.05 K sample showed no discernible D- or G-bands, confirming that potassium promotion effectively suppresses surface carbon deposition during the RWGS reaction. The BET surface area of the catalysts before and after the RWGS reaction is presented in Table S3 of Supplementary Information File. The bare ZrO_2 exhibited a surface area of 48 $m^2.g^{-1}$, which remained nearly unchanged after the reaction, indicating its structural stability under the applied conditions. The incorporation of Fe slightly decreased the surface area to 45 $m^2.g^{-1}$, suggesting partial coverage of the ZrO_2 surface by Fe species. Upon K promotion, the surface area values were largely retained, with 2.5Fe0.05 K and 2.5Fe0.10 K showing 48 and 48.3 $m^2\ g^{-1}$, respectively. The minimal variation between calcined and spent samples across all compositions signifies that the catalysts maintained their textural integrity during the reaction. This stability implies that neither Fe sintering nor extensive carbon deposition occurred under the reaction conditions.

The Thermogravimetric analysis (TGA) profiles of ZrO_2, 2.5FeZr, 2.5Fe0.05 K, and spent 2.5Fe0.05 K catalysts are presented in Fig. S11 of Supplementary Information File. All samples exhibit a minor weight loss below 150 °C, which is attributed to the removal of physiosorbed water and surface hydroxyl groups. A gradual decrease in sample weight continues up to approximately 700 °C, corresponding to the loss of strongly bound surface oxygen species and residual surface functionalities [64].

Notably, the spent 2.5Fe0.05 K catalyst displays a thermal profile nearly identical to its fresh counterpart, with no additional weight loss at elevated temperatures. The absence of any pronounced mass reduction above 500 °C confirms that no carbonaceous species or coke deposits accumulated on the catalyst surface during the reaction. This observation highlights the role of potassium in mitigating carbon formation and preserving catalyst cleanliness under the applied reaction conditions.

3.9. Stability test

The long-term stability of the ZrO_2 supported 2.5Fe0.05 K catalyst during the RWGS reaction at 550 °C was evaluated for 48 h under continuous operation, and the results are shown in Fig. 7. The catalyst maintained a steady CO_2 conversion of approximately 17.2%, with a corresponding CO yield close to the CO_2 conversion. Specifically, 98% of its initial activity is retained and the selectivity towards CO remains >99%. The carbon balance remained nearly constant, and it was well below 0.5%, indicating the absence of measurable carbon accumulation or deactivation over time.

This catalytic stability is corroborated by the TGA analysis, where the spent 2.5Fe0.05 K sample exhibited a thermal profile identical to the fresh catalyst, with no discernible weight loss at high temperatures. The combined evidence unambiguously confirms the absence of carbonaceous deposits after reaction and highlights the effectiveness of potassium promotion in suppressing coke formation, thereby ensuring the structural and catalytic integrity of the Fe–K/ZrO_2 system under RWGS conditions.

4. Conclusion

In this study a K-promoted, ZrO_2 supported Fe-based catalyst was developed for RWGS reaction. Using zirconia as a support Fe loading was varied from sub monolayer to above monolayer coverage and it was found near monolayer coverage catalyst, containing 2.5 wt.% Fe as a metal (2.5FeZr), was the most active in terms of CO yield. The monolayer coverage of Fe over this ZrO_2 support is between 5.03 – 6.0 $atoms_{Fe}/nm^2$. The activity was further improved by addition of potassium as promoter. A small amount of K (K/Fe= 0.05–0.20) was co-impregnated, and it was found that addition of K enhances the reducible amount of Fe-oxide. The optimum ratio lies between K/Fe = 0.05–0.10 molar ratio. It shows that a very small amount of K enhances activity, beyond that limit it starts covering the active sites and hence reduces activity. The addition of K not only increases its activity for the RWGS reaction (from ~14.5% CO_2 conversion for 2.5FeZr to ~17.2% for 2.5Fe0.05 K) but also reduces the difference between CO_2 conversion and CO yield, which shows that it reduces the side products/ carbon deposition. The 2.5Fe0.05 K was also tested for its stability for 48 h, it retains its >98% of its initial activity and the selectivity towards CO was >99% during the process.

CRediT authorship contribution statement

Rajvikram Singh: Writing – review & editing, Writing – original

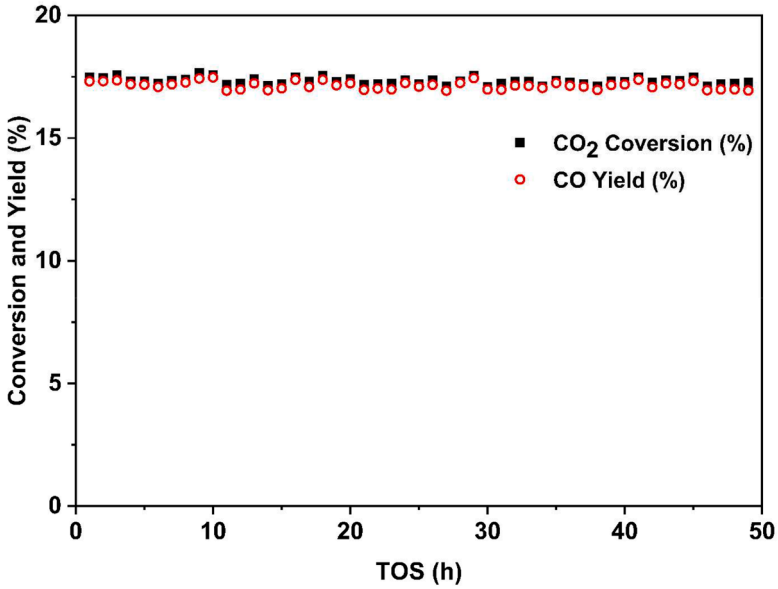

Fig. 7. CO_2 conversion and CO yield during the RWGS reaction at 550 °C over the ZrO_2 supported 2.5Fe0.05 K catalyst, showing stable performance over 48 h of continuous operation. Reaction conditions: $T = 550\ ^{\circ}C$ *and* $P_{H_2} = P_{CO_2} = 0.10\ atm.$ *and* $w = 50\ mg_{cat}$.

draft, Methodology, Investigation, Formal analysis, Data curation, Conceptualization. **Welman C. Elias:** Resources, Investigation, Data curation. **Byeong Jun Cha:** Resources, Data curation. **Raghvendra Singh:** Writing – review & editing, Supervision, Project administration. **Michael S. Wong:** Writing – review & editing, Supervision, Resources, Project administration, Funding acquisition. **Goutam Deo:** Writing – review & editing, Supervision, Resources, Project administration, Investigation, Funding acquisition, Formal analysis, Conceptualization.

Declaration of competing interest

The authors declare that they have no known competing financial interests or personal relationships that could have appeared to influence the work reported in this paper.

Acknowledgement

The authors acknowledge IIT Kanpur, RICE University, RICE-Mehta Fellowship program and Ministry of Education of India for their support.

Supplementary materials

Supplementary material associated with this article can be found, in the online version, at doi:10.1016/j.mcat.2026.116190.

Data availability

Data will be made available on request.

References

[1] S. Anandakrishnan, G.A. Catania, R.B. Alley, H.J. Horgan, Discovery of till deposition at the grounding line of Whillans ice stream, Science 315 (2007) 1835–1838, https://doi.org/10.1126/science.1138393.

[2] P. Friedlingstein, M. O'Sullivan, M.W. Jones, R.M. Andrew, J. Hauck, P. Landschützer, C. Le Quéré, H. Li, I.T. Luijkx, A. Olsen, G.P. Peters, W. Peters, J. Pongratz, C. Schwingshackl, S. Sitch, J.G. Canadell, P. Ciais, R.B. Jackson, S. R. Alin, A. Arneth, V. Arora, N.R. Bates, M. Becker, N. Bellouin, C.F. Berghoff, H. C. Bittig, L. Bopp, P. Cadule, K. Campbell, M.A. Chamberlain, N. Chandra, F. Chevallier, L.P. Chini, T. Colligan, J. Decayeux, L. Djeutchouang, X. Dou, C. D. Rojas, K. Enyo, W. Evans, A. Fay, R.A. Feely, D.J. Ford, A. Foster, T. Gasser, M. Gehlen, T. Gkritzalis, G. Grassi, L. Gregor, N. Gruber, Ö. Gürses, I. Harris, M. Hefner, J. Heinke, G.C. Hurtt, Y. Iida, T. Ilyina, A.R. Jacobson, A. Jain, T. Jarníková, A. Jersild, F. Jiang, Z. Jin, E. Kato, R.F. Keeling, K. Klein Goldewijk, J. Knauer, J.I. Korsbakken, S.K. Lauvset, N. Lefèvre, Z. Liu, J. Liu, L. Ma, S. Maksyutov, G. Marland, N. Mayot, P. McGuire, N. Metzl, N.M. Monacci, E. J. Morgan, S.-I. Nakaoka, C. Neill, Y. Niwa, T. Nützel, L. Olivier, T. Ono, P. I. Palmer, D. Pierrot, Z. Qin, L. Resplandy, A. Roobaert, T.M. Rosan, C. Rödenbeck, J. Schwinger, T.L. Smallman, S. Smith, R. Sospedra-Alfonso, T. Steinhoff, Q. Sun, A. J. Sutton, R. Séférian, S. Takao, H. Tatebe, H. Tian, B. Tilbrook, O. Torres, E. Tourigny, H. Tsujino, F. Tubiello, G. van der Werf, R. Wanninkhof, X. Wang, D. Yang, X. Yang, Z. Yu, W. Yuan, X. Yue, S. Zaehle, N. Zeng, J. Zeng, Glob. Carbon Budg. 2024 (2024), https://doi.org/10.5194/essd-2024-519.

[3] N.L. Panwar, S.C. Kaushik, S. Kothari, Role of renewable energy sources in environmental protection: a review, Renew. Sustain. Energy Rev. 15 (2011) 1513–1524, https://doi.org/10.1016/j.rser.2010.11.037.

[4] C. Hepburn, E. Adlen, J. Beddington, E.A. Carter, S. Fuss, N.M. Dowell, J.C. Minx, P. Smith, C.K. Williams, The technological and economic prospects for CO2 utilization and removal, Nature 575 (2019) 87–97, https://doi.org/10.1038/s41586-019-1681-6.

[5] L. Jeffry, M.Y. Ong, S. Nomanbhay, M. Mofijur, M. Mubashir, P.L. Show, Greenhouse gases utilization: a review, Fuel 301 (2021) 121017, https://doi.org/10.1016/j.fuel.2021.121017.

[6] Z. Turakulov, A. Kamolov, A. Norkobilov, M. Variny, G. Díaz-Sainz, L. Gómez-Coma, M. Fallanza, Assessing various CO2 utilization technologies: a brief comparative review, J. Chem. Technol. Biotechnol. 99 (2024) 1291–1307, https://doi.org/10.1002/jctb.7606.

[7] A. Saravanan, P. Senthil kumar, D.V.N. Vo, S. Jeevanantham, V. Bhuvaneswari, V. Anantha Narayanan, P.R. Yaashikaa, S. Swetha, B. Reshma, A comprehensive review on different approaches for CO2 utilization and conversion pathways, Chem. Eng. Sci. 236 (2021) 116515, https://doi.org/10.1016/j.ces.2021.116515.

[8] M.E. Dry, High quality diesel via the Fischer-Tropsch process - a review, J. Chem. Technol. Biotechnol. 77 (2002) 43–50, https://doi.org/10.1002/jctb.527.

[9] M. Liu, Y. Yi, L. Wang, H. Guo, A. Bogaerts, Hydrogenation of carbon dioxide to value-added chemicals by heterogeneous catalysis and plasma catalysis, Catalysts 9 (2019) 275, https://doi.org/10.3390/catal9030275.

[10] S. Bargigli, M. Raugei, S. Ulgiati, Comparison of thermodynamic and environmental indexes of natural gas, syngas and hydrogen production processes. Energy, Elsevier Ltd, 2004, pp. 2145–2159, https://doi.org/10.1016/j.energy.2004.03.018.

[11] M.T. Luu, D. Milani, A. Bahadori, A. Abbas, A comparative study of CO2 utilization in methanol synthesis with various syngas production technologies, J. CO2. Util. 12 (2015) 62–76, https://doi.org/10.1016/j.jcou.2015.07.001.

[12] M. Ziemba, J. Weyel, C. Hess, Elucidating the mechanism of the reverse water–gas shift reaction over Au/CeO2 catalysts using operando and transient spectroscopies, Appl. Catal. B 301 (2022) 120825, https://doi.org/10.1016/j.apcatb.2021.120825.

[13] X. Chen, X. Su, B. Liang, X. Yang, X. Ren, H. Duan, Y. Huang, T. Zhang, Identification of relevant active sites and a mechanism study for reverse water gas shift reaction over Pt/CeO2 catalysts, J. Energy Chem. 25 (2016) 1051–1057, https://doi.org/10.1016/j.jechem.2016.11.011.

[14] J.H. Kwak, L. Kovarik, J. Szanyi, Heterogeneous catalysis on atomically dispersed supported metals: CO 2 reduction on multifunctional Pd catalysts, ACS. Catal. 3 (2013) 2094–2100, https://doi.org/10.1021/cs4001392.

[15] Y. Tang, C. Asokan, M. Xu, G.W. Graham, X. Pan, P. Christopher, J. Li, P. Sautet, Rh single atoms on TiO2 dynamically respond to reaction conditions by adapting their site, Nat. Commun. 10 (2019), https://doi.org/10.1038/s41467-019-12461-6.
[16] D. Heyl, U. Rodemerck, U. Bentrup, Mechanistic study of low-temperature CO2 hydrogenation over modified Rh/Al2O3 catalysts, ACS. Catal. 6 (2016) 6275–6284, https://doi.org/10.1021/acscatal.6b01295.
[17] L. Pastor-Pérez, F. Baibars, E. Le Sache, H. Arellano-García, S. Gu, T.R. Reina, CO2 valorisation via Reverse Water-Gas Shift reaction using advanced Cs doped Fe-Cu/Al2O3 catalysts, J. CO2. Util. 21 (2017) 423–428, https://doi.org/10.1016/j.jcou.2017.08.009.
[18] M. Wang, G. Zhang, J. Zhu, W. Li, J. Wang, K. Bian, Y. Liu, F. Ding, C. Song, X. Guo, Unraveling the tunable selectivity on cobalt oxide and metallic cobalt sites for CO2 hydrogenation, Chem. Eng. J. 446 (2022) 137217, https://doi.org/10.1016/j.cej.2022.137217.
[19] Y. Tao, Y. Zhu, C. Liu, H. Yue, J. Ji, S. Yuan, W. Jiang, B. Liang, A highly selective Cr/ZrO2 catalyst for the reverse water-gas shift reaction prepared from simulated Cr-containing wastewater by a photocatalytic deposition process with ZrO2, J. Environ. Chem. Eng. 6 (2018) 6761–6770, https://doi.org/10.1016/j.jece.2018.10.043.
[20] H.C. Wu, Y.C. Chang, J.H. Wu, J.H. Lin, I.K. Lin, C.S. Chen, Methanation of CO2 and reverse water gas shift reactions on Ni/SiO2 catalysts: the influence of particle size on selectivity and reaction pathway, Catal. Sci. Technol. 5 (2015) 4154–4163, https://doi.org/10.1039/c5cy00667h.
[21] F. Li, Y. Liu, Y. He, G. Gao, X. Yang, Unlocking the potential of zero-valent single-atom zinc for high-performance reverse water gas shift catalysis, Chem. Eng. J. 521 (2025) 166786, https://doi.org/10.1016/j.cej.2025.166786.
[22] C. Panaritis, J. Zgheib, S.A.H. Ebrahim, M. Couillard, E.A. Baranova, Electrochemical in-situ activation of Fe-oxide nanowires for the reverse water gas shift reaction, Appl. Catal. B 269 (2020) 118826, https://doi.org/10.1016/j.apcatb.2020.118826.
[23] J.A. Loiland, M.J. Wulfers, N.S. Marinkovic, R.F. Lobo, Fe/γ-Al2O3 and Fe-K/γ-Al2O3 as reverse water-gas shift catalysts, Catal. Sci. Technol. 6 (2016) 5267–5279, https://doi.org/10.1039/c5cy02111a.
[24] B. Zhou, Y. Xie, C. Wang, K. Li, S. Bao, X. Sun, X. Huang, P. Ning, K. Li, L. Shi, F. Wang, The key role of catalyst structure adjustment and optimization in the reverse water-gas shift reaction, Green Carbon. 4 (2026) 126–141, https://doi.org/10.1016/j.greenca.2025.08.004.
[25] J.M. Arce-Ramos, W.Q. Li, S.H. Lim, J. Chang, T. Hashimoto, H. Kamata, M. B. Sullivan, A. Borgna, L. Chen, C.K. Poh, J. Zhang, Investigating the deactivation and regeneration mechanism of Fe-based catalysts during CO2 reduction to chemicals, Appl. Catal. B 347 (2024) 123794, https://doi.org/10.1016/j.apcatb.2024.123794.
[26] D. Xu, H. Fan, K. Liu, G. Hou, C. Qin, Y. Xu, R. Li, J. Wang, M. Ding, Impacts of interaction between active components on catalyst deactivation over KFe/ZSM-5 bifunctional catalyst, ACS. Sustain. Chem. Eng. 11 (2023) 10441–10452, https://doi.org/10.1021/acssuschemeng.3c01826.
[27] C.M. Kalamaras, D.D. Dionysiou, A.M. Efstathiou, Mechanistic studies of the water-gas shift reaction over Pt/Ce xZr1-xO2 catalysts: the effect of Pt particle size and Zr dopant, ACS. Catal. 2 (2012) 2729–2742, https://doi.org/10.1021/cs3006204.
[28] M. González-Castano, J.C. Navarro De Miguel, F. Sinha, S. Ghomsi Wabo, O. Klepel, H. Arellano-Garcia, Cu supported Fe-SiO2nanocomposites for reverse water gas shift reaction, J. CO2. Util. 46 (2021) 101493, https://doi.org/10.1016/j.jcou.2021.101493.
[29] A.A. Isah, O. Ohiro, L. Li, Y. Nasiru, K.C. Szeto, P.Y. Dugas, A. Benayad, A. De Mallmann, S.L. Scott, B.R. Goldsmith, M. Taoufik, Selective catalytic reduction of CO2 to CO by a single-site heterobimetallic iron-potassium complex supported on alumina, ACS. Catal. 14 (2024) 2418–2428, https://doi.org/10.1021/acscatal.3c04989.
[30] F. Qian, M. Wang, Z. Wei, Y. Cai, Z. Sun, R. Liang, G. Liu, M. Qing, H. Wang, J. Liu, X.W. Liu, Y. Yang, X.D. Wen, Stabilized Fe7C3 catalyst with K–Mg dual promotion for robust CO2 hydrogenation to high-value olefins, Nat. Commun. 16 (2025), https://doi.org/10.1038/s41467-025-63218-3.
[31] M.S. Wong, D.M. Antonelli, J.Y. Ying, Pn S0965-9773(97)00044-$ synthesis and characterization of phosphated mesoporous zirconium oxide, Nanostruct. Mater. 9 (1997) 165–168, https://doi.org/10.1016/S0965-9773(97)00044-5.
[32] K. Hong, W.C. Elias, K.N. Heck, T. Terlier, D. Dimpel, W. Qian, B. Liu, T. Kurihara, M.S. Wong, Pulsed laser ablation-synthesized FePt nanoparticles have enhanced catalytic nitrite reduction activity, Catal. Today 453 (2025) 115254, https://doi.org/10.1016/j.cattod.2025.115254.
[33] L. Duan, B. Wang, K.N. Heck, C.A. Clark, J. Wei, M. Wang, J. Metz, G. Wu, A. L. Tsai, S. Guo, J. Arredondo, A.D. Mohite, T.P. Senftle, P. Westerhoff, P. Alvarez, X. Wen, Y. Song, M.S. Wong, Titanium oxide improves boron nitride photocatalytic degradation of perfluorooctanoic acid, Chem. Eng. J. 448 (2022) 137735, https://doi.org/10.1016/j.cej.2022.137735.
[34] S. Glass, H. Kannan, J. Bangala, Y. Chen, J. Metz, R. Mowzoon-Mogharrabi, G. Gao, A.K. Meiyazhagan, M.S. Wong, P.M. Ajayan, T.P. Senftle, P.J.J. Alvarez, Iron doping of hBN enhances the photocatalytic oxidative defluorination of perfluorooctanoic acid, ACS. Appl. Mater. Interfaces. 17 (2025) 22803–22811, https://doi.org/10.1021/acsami.5c01963.
[35] H.P. Jacobs, W.C. Elias, K.N. Heck, D.P. Dean, J.J. Dodson, W. Zhang, K. Hong, J. H. Arredondo, C.J. Breckner, L. Chen, S.G. Mueller, S.R. Alexander, J.T. Miller, M. S. Wong, Promotional role of acid sites on aluminosilicate-supported PdAu for vinyl acetate synthesis, ACS. Catal. 14 (2024) 211–226, https://doi.org/10.1021/acscatal.3c04335.
[36] N. Soultanidis, W. Zhou, C.J. Kiely, M.S. Wong, Solvothermal synthesis of ultrasmall tungsten oxide nanoparticles, Langmuir 28 (2012) 17771–17777, https://doi.org/10.1021/la3029462.
[37] S.S. Chan, I.E. Wachs, L.L. Murrell, L. Wang, W.K. Hall, In situ laser raman spectroscopy of supported metal oxides. https://pubs.acs.org/sharingguidelines, 1984.
[38] X. Cui, S.K. Kær, Thermodynamic analyses of a moderate-temperature process of carbon dioxide hydrogenation to methanol via reverse water-gas shift with in situ water removal, Ind. Eng. Chem. Res. 58 (2019) 10559–10569, https://doi.org/10.1021/acs.iecr.9b01312.
[39] M. Cherian, M.S. Rao, A.M. Hirt, I.E. Wachs, G. Deo, Oxidative dehydrogenation of propane over supported chromia catalysts: influence of oxide supports and chromia loading, J. Catal. 211 (2002) 482–495, https://doi.org/10.1006/jcat.2002.3759.
[40] T.V. Malleswara Rao, G. Deo, J.M. Jehng, I.E. Wachs, In situ UV-vis-NIR diffuse reflectance and raman spectroscopy and catalytic activity studies of propane oxidative dehydrogenation over supported CrO 3/ZrO 2 catalysts, Langmuir 20 (2004) 7159–7165, https://doi.org/10.1021/la049590v.
[41] R. Singh, R. Singh, G. Deo, Developing a supported metal oxide catalyst for direct dehydrogenation of propane to propene, Appl. Catal. Gen. 703 (2025) 120354, https://doi.org/10.1016/j.apcata.2025.120354.
[42] J. Liang, X. Jiang, G. Liu, Z. Deng, J. Zhuang, F. Li, Y. Li, Characterization and synthesis of pure ZrO 2 nanopowders via sonochemical method, Mater. Res. Bull. 38 (2003) 161–168, https://doi.org/10.1016/S0025-5408(02)01007-3.
[43] N. Chandra, D.K. Singh, M. Sharma, R.K. Upadhyay, S.S. Amritphale, S.K. Sanghi, Synthesis and characterization of nano-sized zirconia powder synthesized by single emulsion-assisted direct precipitation, J. Colloid. Interface Sci. 342 (2010) 327–332, https://doi.org/10.1016/j.jcis.2009.10.065.
[44] R.D. Purohit, S. Saha, A.K. Tyagi, Combustion synthesis of nanocrystalline ZrO2 powder: XRD, raman spectroscopy and TEM studies, Mater. Sci. Eng. B 130 (2006) 57–60, https://doi.org/10.1016/j.mseb.2006.02.041.
[45] D.G. Lamas, A.M. Rosso, M.S. Anzorena, A. Fernández, M.G. Bellino, M.D. Cabezas, N.E. Walsöe de Reca, A.F. Craievich, Crystal structure of pure ZrO2 nanopowders, Scr. Mater. 55 (2006) 553–556, https://doi.org/10.1016/j.scriptamat.2006.05.035.
[46] M. Farahmandjou, F. Soflaee, Synthesis and characterization of α-Fe2O3 nanoparticles by simple co-precipitation method, Phys. Chem. Res. 3 (2015) 191–196, https://doi.org/10.22036/pcr.2015.9193.
[47] O.M. Lemine, Microstructural characterisation of α - Fe2 O3 nanoparticles using, XRD line profiles analysis, FE-SEM and FT-IR, Superlattices. Microstruct. 45 (2009) 576–582, https://doi.org/10.1016/j.spmi.2009.02.004.
[48] Y. Okamoto, T. Kubota, Y. Ohto, S. Nasu, Metal oxide-support interactions in Fe/ZrO2 calaysts, J. Phys. Chem. B 104 (2000) 8462–8470, https://doi.org/10.1021/jp994122t.
[49] T.C. Peck, G.K. Reddy, M. Jones, C.A. Roberts, Monolayer detection of supported Fe and Co oxides on ceria to establish structure-activity relationships for reduction of NO by CO, J. Phys. Chem. C 121 (2017) 8435–8443, https://doi.org/10.1021/acs.jpcc.7b00398.
[50] T. Herranz, S. Rojas, F.J. Pérez-Alonso, M. Ojeda, P. Terreros, J.L.G. Fierro, Carbon oxide hydrogenation over silica-supported iron-based catalysts. Influence of the preparation route, Appl. Catal. Gen. 308 (2006) 19–30, https://doi.org/10.1016/j.apcata.2006.04.007.
[51] M.S. Kumar, M. Schwidder, W. Grünert, A. Brückner, On the nature of different iron sites and their catalytic role in Fe-ZSM-5 DeNOx catalysts: new insights by a combined EPR and UV/VIS spectroscopic approach, J. Catal. 227 (2004) 384–397, https://doi.org/10.1016/j.jcat.2004.08.003.
[52] A. Gervasini, C. Messi, A. Ponti, S. Cenedese, N. Ravasio, Nanodispersed Fe oxide supported catalysts with tuned properties, J. Phys. Chem. C 112 (2008) 4635–4642, https://doi.org/10.1021/jp710742g.
[53] J. Gurgul, K. Łątka, I. Hnat, J. Rynkowski, S. Dzwigaj, Identification of iron species in FeSiBEA by DR UV-vis, XPS and mössbauer spectroscopy: influence of Fe content, Microporous Mesoporous Mater. 168 (2013) 1–6, https://doi.org/10.1016/j.micromeso.2012.09.015.
[54] J. Kumar Prabhakar, P.A. Apte, G. Deo, The kinetics of Ni/Al2O3 and Ni-Fe/Al2O3 catalysts for the CO2 methanation reaction and the reasons for promotion, Chem. Eng. J. 471 (2023) 144252, https://doi.org/10.1016/j.cej.2023.144252.
[55] D. Pandey, K. Ray, R. Bhardwaj, S. Bojja, K.V.R. Chary, G. Deo, Promotion of unsupported nickel catalyst using iron for CO2 methanation, Int. J. Hydrog. Energy 43 (2018) 4987–5000, https://doi.org/10.1016/j.ijhydene.2018.01.144.
[56] R. Singh, R. Singh, G. Deo, Developing a supported metal oxide catalyst for direct dehydrogenation of propane to propene, Appl. Catal. Gen. 703 (2025) 120354, https://doi.org/10.1016/j.apcata.2025.120354.
[57] J.M. Arana Juve, X. Baami González, L. Bai, Z. Xie, Y. Shang, A. Saad, R. Gonzalez-Olmos, M.S. Wong, M. Ateia, Z. Wei, Size-selective trapping and photocatalytic degradation of PFOA in Fe-modified zeolite frameworks, Appl. Catal. B 349 (2024) 123885, https://doi.org/10.1016/j.apcatb.2024.123885.
[58] Y. Joseph, G. Ketteler, C. Kuhrs, W. Ranke, W. Weiss, R. Schlögl, On the preparation and composition of potassium promoted iron oxide model catalyst films, Phys. Chem. Chem. Phys. 3 (2001) 4141–4153, https://doi.org/10.1039/b104263g.
[59] Z. Gou, C. Huang, G. Zhou, X. Ren, L. Deng, T. Wang, Q. Peng, Coupling and electronic synergistic effects of Fe/CeO2 composite to achieve high efficiency and selectivity for RWGS reaction, J. CO2. Util. 81 (2024) 102728, https://doi.org/10.1016/j.jcou.2024.102728.
[60] Q. Zhang, L. Pastor-Pérez, Q. Wang, T. Ramirez Reina, Conversion of CO2 to added value products via rWGS using Fe-promoted catalysts: carbide, metallic Fe or a

mixture? J. Energy Chem. 66 (2022) 635–646, https://doi.org/10.1016/j.jechem.2021.09.015.
[61] D.H. Kim, S.W. Han, H.S. Yoon, Y.D. Kim, Reverse water gas shift reaction catalyzed by Fe nanoparticles with high catalytic activity and stability, J. Ind. Eng. Chem. 23 (2015) 67–71, https://doi.org/10.1016/j.jiec.2014.07.043.
[62] L. Yang, L. Pastor-Pérez, J.J. Villora-Pico, A. Sepúlveda-Escribano, F. Tian, M. Zhu, Y.F. Han, T. Ramirez Reina, Highly active and selective multicomponent Fe-Cu/CeO2-Al2O3 catalysts for CO2 upgrading via RWGS: impact of Fe/Cu ratio, ACS. Sustain. Chem. Eng. 9 (2021) 12155–12166, https://doi.org/10.1021/acssuschemeng.1c03551.
[63] S. Sengupta, A. Jha, P. Shende, R. Maskara, A.K. Das, Catalytic performance of Co and Ni doped Fe-based catalysts for the hydrogenation of CO 2 to CO via reverse water-gas shift reaction, J. Environ. Chem. Eng. 7 (2019) 102911, https://doi.org/10.1016/j.jece.2019.102911.
[64] S. Gupta, S. Tiwari, V.K. Arghode, G. Deo, Cobalt promotion and Ni+Co loading effects of γ-Al2O3-supported Ni-Co catalysts for the flue gas reforming of methane, Energy Fuels. 38 (2024) 11022–11036, https://doi.org/10.1021/acs.energyfuels.4c01317.